Solid-State Materials for Clean Energy: Insights from Atomic-Scale Modeling

M. Saiful Islam and Peter R. Slater

Abstract

Fundamental advances in solid-state ionics for energy conversion and storage are crucial in addressing the global challenge of cleaner energy sources. This review aims to demonstrate the valuable role that modern computational techniques now play in providing deeper fundamental insight into materials for solid oxide fuel cells and rechargeable lithium batteries. The scope of contemporary work is illustrated by studies on topical materials encompassing perovskite-type proton conductors, gallium oxides with tetrahedral moieties, apatite-type silicates, and lithium iron phosphates. Key fundamental properties are examined, including mechanisms of ion migration, dopant-defect association, and surface structures and crystal morphologies.

Introduction

One of the major challenges in the 21st century is the development of cleaner, sustainable sources of energy to deal with the environmental threat of global warming and the declining reserves of fossil fuels. A range of energy conversion and storage technologies, including fuel cells and lithium batteries, are being developed to help cut carbon emissions.

The performance of these energy systems depends crucially on the properties of their component materials. Indeed, innovative materials chemistry lies at the center of advances that have already been made in this field,[1] an excellent example being the rechargeable lithium battery, which has helped power the revolution in portable electronics.

This review addresses new materials for two important "green" technologies: first, solid oxide fuel cells (SOFCs), which are suitable for combined heat and power generation in homes and other stationary applications;[2,3] and second, rechargeable lithium batteries, which are essential to meet the requirements of future portable consumer equipment and hybrid electric vehicles.[4–7]

For the next generation of energy devices, the discovery and optimization of high-performance materials are critical to future breakthroughs. This depends on exploring new classes of compounds and a better understanding of the fundamental science of ionically conducting solids (solid-state ionics) that underpin applied research. However, an atomic-scale understanding of the defect properties and conduction mechanisms in new complex systems is often lacking.

Computer modeling techniques are now well-established tools in this field of solid-state ionics and have been applied successfully to studies of structures and dynamics of solids on the atomic- and nanoscale. A major theme of modeling work has been the strong interaction with experimental studies. The principal aims of computer modeling are (1) to complement and assist in the interpretation of experimental studies (e.g., diffraction, conductivity); (2) to investigate atomic-scale features (e.g., conduction paths, point defects, lithium insertion sites) that may be difficult to extract from experiment alone; and (3) to have a predictive role in the improvement of materials.

Although several examples of the studies of others will be mentioned, it is beyond the scope of this review to give an exhaustive summary of all the excellent work in this highly active field. Rather, this review focuses on efforts to address recent progress in computational studies of ionic transport, defect chemistry, and surface properties of topical materials. In particular, we highlight contemporary work on ion conductors for SOFCs (such as perovskite oxides and apatite silicates) and on cathode materials for lithium batteries (such as iron phosphate) to illustrate the breadth of information that can be obtained.

Computational Methods

Our description of the computational techniques will be brief because comprehensive reviews are given elsewhere.[8–11] In general, three main classes of technique have been employed in the study of solid-state ionic materials: atomistic (static lattice), molecular dynamics (MD), and quantum mechanical (*ab initio*) methods.

First, atomistic simulation methods[8] determine the lowest energy configuration of the crystal structure by employing efficient energy minimization procedures. The calculations rest upon the specification of an interatomic potential model, which expresses the total energy of the system as a function of the nuclear coordinates. For solid-state ionics, the Born model framework is commonly employed, which partitions the total energy into long-range Coulombic interactions, and a short-range term is given to model the repulsions and van der Waals forces between electron charge clouds. The shell model, in which charge separation can occur between the ionic core and a massless shell connected by a harmonic spring, provides a simple description of polarizibility effects and has proven to be effective in simulating dielectric and lattice dynamical properties. It should be stressed, as argued previously,[8] that employing such a potential model does not necessarily mean that the electron distribution corresponds to a fully ionic system, and that the general validity of the model is assessed primarily by its ability to reproduce observed properties of the crystal lattice, such as unit cell parameters.

An important feature of these calculations is the treatment of lattice relaxation (using the Mott-Littleton approach[8,10]) around the point defect, dopant cluster, or migrating ion, so the crystal is not considered simply as a rigid lattice. This method partitions a crystal lattice into two regions, with ions within the inner spherical region (>500 ions) immediately surrounding the defect relaxed explicitly. Relaxation of such a large number of ions is important for charged defects that introduce long-range

electrostatic perturbations and is not easily treated by electronic structure methods. The outer region extends to infinity, with the outer lattice relaxation treated by quasi-continuum methods, since the defect forces here are relatively weak. These methods are embodied in the GULP (General Utility Lattice Program) simulation code.[10] The atomistic modeling of surface structures and energies uses similar methodology to bulk calculations, describing the crystal as a stack of planes periodic in two dimensions.

The second main type of simulation method is the MD technique,[8,11] which consists of an explicit dynamical simulation of the ensemble of particles for which Newton's equations of motion are solved numerically. As before, classical interatomic potentials are also used to treat the forces, with repetition of the integration algorithm yielding a detailed picture of the evolution of ion positions and velocities as a function of time. A widely used MD code is the DL_POLY program, developed at Daresbury Laboratory in the UK.[11]

Finally, we note that there is an expanding role for quantum mechanical or *ab initio* methods to provide information on the electronic structure of the solid. Techniques based on density functional theory (DFT) are now increasingly viewed as an important approach in materials science, with the exchange-correlation energy being treated by the local density approximation or the generalized-gradient approximation (incorporated in the VASP[12] and CASTEP[13] packages). There is also the use of hybrid exchange functionals (such as B3LYP) within DFT. Hybrid functionals are a class of approximations to the exchange-correlation energy functional in DFT that incorporate a portion of exact exchange from Hartree-Fock theory.[9]

A widely used implementation of DFT combines a plane-wave basis set with the "pseudopotential" method, in which the pseudopotential replaces the core electrons by an effective potential in which the valence electron states can evolve. More recently, there is the use of DFT+U for open-shell transition metal compounds, where U is the on-site Coulomb interaction parameter. So-called *ab initio* molecular dynamics can be obtained by using the Hellman-Feynman theorem;[9] this theorem allows the calculation of interatomic forces and assumes classical behavior for the nuclei, which evolve adiabatically on the electronic potential energy surface.

The starting point for the computational work, prior to the investigation of defects and transport, was the simulation of the equilibrium bulk structures. The calculated and experimental unit cell parameters for the materials discussed in this review are listed in Table I. Examination of the values shows good agreement between experimental and simulated structures. This provides a reliable starting point for the subsequent simulations.

Ion Conductors for Solid Oxide Fuel Cells

There is considerable interest in solid oxide fuel cells (SOFCs) due to their high efficiency and ability to act as a bridging technology between hydrocarbon and hydrogen fuel systems.[2,3] There is also significant activity[2,3] in developing alternative ion conductors to the conventional Y/ZrO_2 electrolyte to operate at lower temperatures (500–700°C) for so-called intermediate-temperature SOFCs. These include Bi-based oxides (e.g., doped Bi_2O_3, doped $Bi_4V_2O_{11}$, or BIMEVOX, where BI is bismuth, ME is metal, V is vanadium, and OX is oxygen), perovskites (e.g., $LaGaO_3$, $CaZrO_3$), K_2NiF_4-type oxides (e.g., $La_2NiO_{4+\delta}$), and apatite silicates (e.g., $La_{9.33}Si_6O_{26}$).[2,3] To demonstrate recent progress in simulation studies in this area, we have selected three important systems that highlight different mechanistic features.

Perovskite Oxides: Proton Transport and Trapping

The perovskite structure can be dubbed an inorganic chameleon since it displays a rich diversity of chemical compositions and properties such as oxide-ion conduction (e.g., doped $LaGaO_3$), colossal magnetoresistance (e.g., $La_{1-x}Sr_xMnO_3$), catalysis (e.g., $LaCoO_3$, $LaFeO_3$), and ferroelectric behavior (e.g., $BaTiO_3$, $BiFeO_3$).[2,3] In addition to oxygen ion conduction, perovskite oxides have received considerable attention as high-temperature proton conductors with promising use in SOFCs.[14,15] Most attention has focused on AMO_3 perovskites (where A and M are 2+ and 4+ cations, respectively), particularly $ACeO_3$ and $AZrO_3$, which are typically acceptor-doped with trivalent ions at the M^{4+} site. When these perovskite oxides are exposed to water vapor, the oxygen vacancies are replaced by hydroxyl groups, described, in Kröger-Vink notation, as follows:

$$H_2O(g) + V_O^{\bullet\bullet} + O_O^x \rightarrow 2OH_O^{\bullet}, \qquad (1)$$

where V indicates a vacancy defect on an oxygen site, and the superscript dots indicate an effective doubly positive charge. The oxygen sits on an oxygen site (subscript O) with a neutral charge (denoted by the superscript x). Similarly, the hydroxide ion sits on an oxygen site with an effective single positive charge (superscript dot). Computational studies based on DFT methodology have allowed the probing of proton transport in the $CaZrO_3$ orthorhombic perovskite (shown in Figure 1) with a high level of microscopic detail.[16] *Ab initio* and MD simulations confirm that

Table I: Comparison of the Calculated and Experimental Unit Cell Parameters of Select Materials.[16,19,33,39]

Compound	Lattice Parameter	Experimental (Å)	Calculated (Å)	Difference (%)
$CaZrO_3$	*a*	5.5912	5.5995	0.15
	b	8.0171	8.0550	0.47
	c	5.7616	5.7667	0.09
$SrCeO_3$	*a*	6.1312	6.0744	–0.93
	b	8.6504	8.5421	–1.25
	c	5.9944	5.9834	–0.18
$La_{9.33}Si_6O_{26}$	*a*,*b*	9.7248	9.7607	0.37
	c	7.1895	7.1198	–0.97
$La_8Sr_2Si_6O_{26}$	*a*,*b*	9.7083	9.8053	1.00
	c	7.2377	7.1558	–1.13
$LaBaGaO_4$	*a*	10.0136	10.0553	0.42
	b	7.2653	7.2522	–0.18
	c	5.9095	5.8722	–0.63
$LiFePO_4$	*a*	10.3377	10.3713	0.33
	b	6.0112	6.0216	0.17
	c	4.6950	4.6695	–0.54

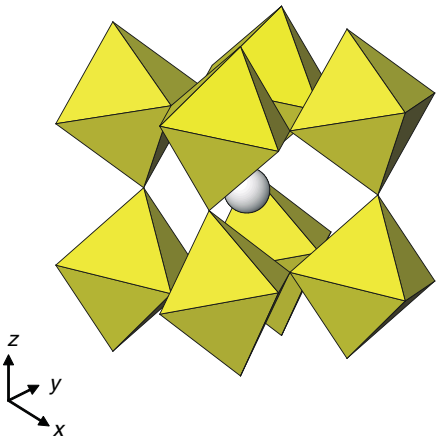

Figure 1. Orthorhombic AMO_3 perovskite structure showing tilting MO_6 octahedra (yellow) and the A cation (grey sphere).

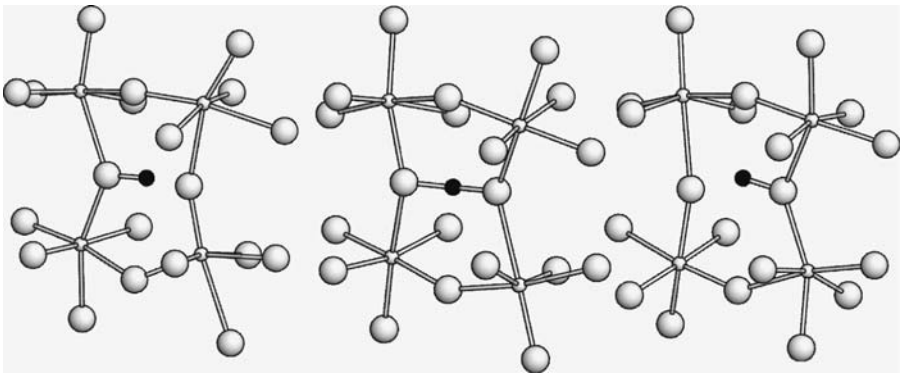

Figure 2. Sequence of snapshots from *ab initio* molecular dynamics simulations showing inter-octahedra proton hopping in perovskite-structured orthorhombic $CaZrO_3$ (Reference 16). Small spheres are Zr; large spheres are O; small black spheres are protons; Ca ions are omitted for clarity.

the diffusion mechanism involves proton transfer from one oxygen ion to the next (Grötthuss-type mechanism), shown in Figure 2. The simulations indicate the importance of vibrational dynamics of the oxygen sublattice and suggest that proton transfer is phonon-assisted. For each hopping event, the oxygen-oxygen separation contracts by about 0.4 Å so as to facilitate proton transfer by stabilizing the barrier state. At this barrier configuration, the calculated electron density shows equal hydrogen bonding to the two oxygen ions, indicating that the proton is not transferred through a totally "free" state.

A very low-energy barrier for proton transfer is found for the inter-octahedra path, influenced by the close oxygen-oxygen separations between tilting octahedra. Long-range proton conduction in $CaZrO_3$ may, however, involve intra-octahedra proton transfer as the rate-limiting step with a calculated energy barrier of 0.74 eV, which agrees with experimental activation energies.

It is well-known that interactions between dopant ions and their charge-compensating defects can lead to the formation of distinct clusters that can trap the migrating species. For example, the oxygen ion conductivity of fluorite-structured oxides (such as Y-doped CeO_2) is strongly affected by the extent of dopant-vacancy interactions.[17,18]

Analogous to dopant-vacancy interactions, the proton also may associate preferentially with dopants, leading to possible trapping. In this context, the binding energy[19] associated with a cluster comprised of an OH group and adjacent trivalent cations (M'_{Ce}–$OH^{\bullet}_{o}$:M on a Ce site with an effective single negative charge; hydroxide sitting on an O site with an effective single positive charge) within the $SrCeO_3$ proton conductor has been calculated. The results are shown in Figure 3 as a function of ionic radius. The negative values for the binding energies indicate that dopant-defect (M'_{Ce}–$OH^{\bullet}_{o}$) pair clusters are favorable. In particular, the magnitudes of the M'_{Ce}–$OH^{\bullet}_{o}$ binding energies are considerably lower for Y^{3+} and Yb^{3+} in comparison to the other dopants.

Since these Y and Yb dopants are most often associated with high protonic conductivity in the $SrCeO_3$ system,[19–21] it follows that the lower conductivity of other doped systems (e.g., Sc) may partly result from appreciable dopant-proton association or trapping. The calculated binding energies given in Figure 3 are also similar to experimental values for proton trapping energies for doped $SrCeO_3$ obtained from QENS (quasielastic neutron scattering) experiments.[22] The atomistic calculations thus support the experimental spectroscopic evidence of proton-dopant association.

The trend found in Figure 3 suggests the importance of ion-size and elastic-strain effects, in addition to electrostatic terms, in which the binding energy is dependent upon the ion size mismatch between host and dopant, and the expectation of a binding energy minimum when the ionic radii are approximately the same. These results and elastic strain arguments are analogous to studies on fluorite-structured oxides[17,18] and to recent work on doped perovskites $LaMO_3$ (M = Ga, Fe).[23,24]

Apatite Silicates: Oxide-Ion Transport

To date, oxide materials exhibiting fluorite or perovskite structures have dominated research on electrolytes for SOFCs.[2,3,17,18] Recently, however, a range of rare-earth apatite materials have been proposed as alternative solid electrolyte materials following the exciting discovery of fast oxide-ion conductivity in these silicate systems.[25–32]

Isostructural with the well-known mineral hydroxyapatite (related to that found in bones and teeth), the silicate-based materials have the general formula $Me_{10}(SiO_4)_6O_{2\pm y}$, where Me is a metal such as a rare-earth or alkaline earth. The crystal structure (shown in Figure 4) comprises isolated SiO_4 tetrahedra arranged so as to form two distinct channels running parallel to the *c*-axis. Occupying the smaller of these channels are Me cations, while the larger channel contains Me and oxide ions.

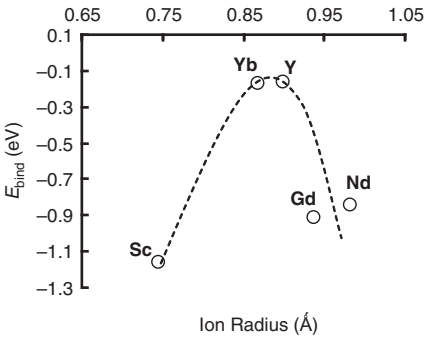

Figure 3. Calculated binding energies E_{bind} of dopant-defect (M'_{Ce} $OH^{\bullet}_{o}$: M sits on a Ce site with an effective single negative charge; OH sits on an O site with an effective single positive charge) pair clusters in the $SrCeO_3$ proton conductor as a function of dopant ionic radius.[59] The dashed line is a guide to the eye illustrating the trend versus ion size.

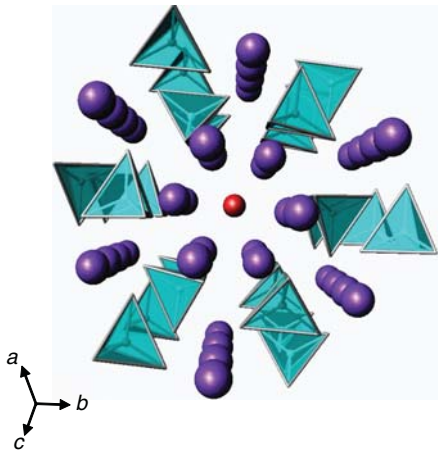

Figure 4. Structure of the apatite-type oxide $La_{10-x}Si_6O_{26}$ showing SiO_4 tetrahedra (blue), La ions (purple), and channel oxygen (red).[28]

Early experimental work indicated the importance of interstitial oxide ions.[26–30] In order to investigate the defect chemistry and conduction mechanism in more detail, atomistic modeling studies[33] were performed for the first time on the two systems: $La_{9.33}(SiO_4)_6O_2$ and $La_8Sr_2(SiO_4)_6O_2$; the former shows high conductivity, while the latter is a poor oxide-ion conductor.

A principal result of this work was that the interstitial oxygen, rather than being located down the channel center as initially thought, was accommodated at the channel periphery. This position is stabilized by the displacement of the nearby silicate unit toward the La channels, accounting for the high thermal displacement parameters observed for the silicate oxygen atoms. Subsequently, the predicted location of this channel periphery site was confirmed by neutron diffraction studies.[28–30]

Additional support for this interstitial oxide-ion site has come from ^{29}Si NMR (nuclear magnetic resonance) studies of a range of alkaline earth-doped apatite silicates.[34] These studies have shown a correlation between the ^{29}Si NMR spectra and the conductivity, with poorly conducting samples demonstrating a single NMR resonance, whereas in fast ion conducting compositions, an extra peak was apparent, attributed to a silicate group adjacent to an interstitial oxygen site.

But how do the oxide ions move? The simulation results suggested that the conduction mechanism in $La_{9.33}(SiO_4)_6O_2$ is via an interstitial mechanism, while that of $La_8Sr_2(SiO_4)_6O_2$ involves a vacancy mechanism, with good correlation between observed and calculated activation energies.[33] The predicted interstitial conduction pathway for $La_{9.33}(SiO_4)_6O_2$ is a complex sinusoidal process, as shown in Figure 5. An important feature is that the conduction process is aided by cooperative displacements of the silicate tetrahedra, suggesting that the flexibility of the silicate substructure is essential to the observed high oxide-ion conductivities.

In the oxygen-excess system, $La_{9.67}(SiO_4)_6O_{2.5}$ migration can be viewed as a handover mechanism, whereby the interstitial oxide ion is passed from one silicate unit to another.[35] More recently, MD simulations[36] of the germanate $La_{9.33}(GeO_4)_6O_2$ indicate that the role of the channel oxygen atoms appears to be as a "reservoir" for the creation of mobile interstitial oxide ions, and that their migration occurs via the GeO_4 tetrahedra, which allows for conduction both parallel and perpendicular to the *c*-axis channel.

The interstitial conduction mechanism in apatites is in contrast to both fluorite and perovskite-type SOFC materials, in which oxide-ion conduction proceeds through vacancy mechanisms. Although not described here, the apatite silicates are highly tolerant to cation doping,[28] which provides new opportunities to optimize their properties as fuel cell electrolytes.

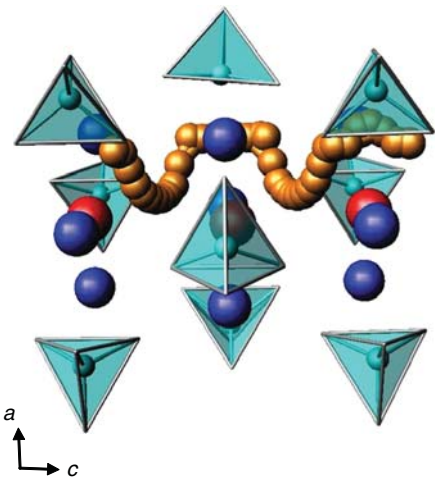

Figure 5. Interstitial oxide-ion migration pathway (gold) in the $La_{9.33}Si_6O_{26}$ apatite, with a view perpendicular to the *c*-axis.[28] SiO_4 tetrahedra (blue), La ions (purple), and channel oxygen (red).

Gallates with Tetrahedral Moieties: Oxide-Ion Transport

There is growing interest in alternative structure types for intermediate-temperature (400–700°C) SOFCs. In particular, structures containing tetrahedral moieties, such as $La_{1-x}Ca_xNbO_{4-x/2}$,[37] $La_{1-x}Ba_{1+x}GaO_{4-x/2}$,[38] and the apatites (discussed previously), have been attracting considerable attention recently. In this context, we have carried out a combined experimental and computational modeling study of the $La_{1-x}Ba_{1+x}GaO_{4-x/2}$ system, which exhibits both proton and oxide-ion conduction.[38]

The structure of $LaBaGaO_4$ is shown in Figure 6, which contains gallium in a distorted tetrahedral environment and ordered alternating layers of lanthanum and barium. Changing the La/Ba ratio produces oxygen vacancies, but how are these anion defects accommodated? Both potential-based and DFT simulations[39] demonstrate that rather than producing three-coordinate Ga units, the oxygen vacancy defects are accommodated by considerable relaxation of a neighboring GaO_4 unit, resulting in the formation of a Ga_2O_7 group, such that each Ga retains its tetrahedral coordination. The prediction of these Ga_2O_7 defects from the modeling work provoked a re-examination of the neutron diffraction data for $La_{0.8}Ba_{1.2}GaO_{3.9}$. Fourier maps were calculated from the neutron diffraction data, with the best fit achieved using a split oxygen (O3) site, consistent with the presence of both an isolated GaO_4 tetrahedron and a Ga_2O_7 unit.

A series of atomistic and MD simulations were used to investigate several possible pathways for oxide-ion migration.[39] The lowest energy pathway (Figure 7) was shown to occur via the breaking and reformation of the Ga_2O_7 units (with an oxide-ion migration energy of 0.6 eV). The transfer of oxide ions between neighboring tetrahedra facilitates long-range diffusion. Thus, rather than inhibiting the conduction process, the Ga_2O_7 units are integral to it.

Therefore, the predicted oxide-ion conduction pathway is unusual and reminiscent of a concerted cogwheel-type motion, with the effective transfer of oxide-ion vacancies facilitated by Ga_2O_7 defects. The process requires significant rotation of the Ga_2O_7 and GaO_4 units, suggesting that the structure is relatively flexible and allows facile rotation of these units.

Similar mechanistic aspects may be featured in the ionic conduction characteristics of related oxide systems (e.g., doped $LaNbO_4$)[37] containing tetrahedral moieties and warrants further experimental and computational investigation.

Cathode Materials for Lithium Batteries

In the field of lithium battery research, there is tremendous activity devoted to finding alternatives to cobalt-oxide cathodes, particularly for potential use in

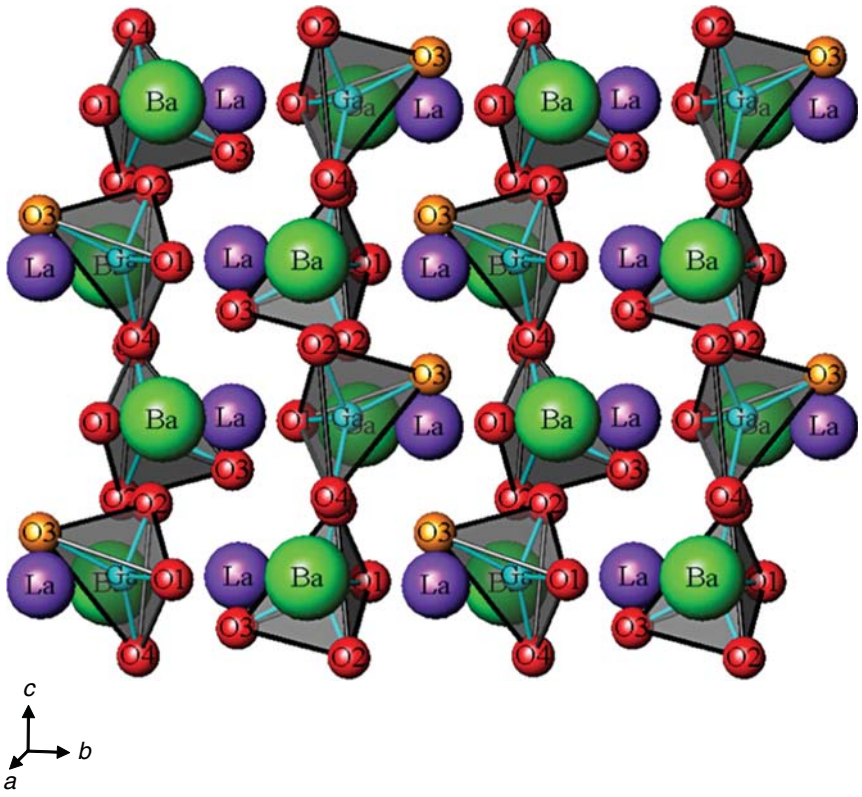

Figure 6. Crystal structure of $LaBaGaO_4$.[39] The structure is unusual in that it contains Ga in isolated distorted tetrahedra; the four non-equivalent oxygens are labeled, and the longest Ga–O bond highlighted, with O3 in orange.

hybrid electric or pure electric vehicles to help reduce CO_2 emissions from road transport.[4–7] Current candidates include Mn- or Fe-based materials, such as layered oxides (e.g., $LiNi_{0.5}Mn_{0.5}O_2$), spinel oxides (e.g., $LiMn_{1.5}Ni_{0.5}O_4$), and polyanionic materials (e.g., $LiFePO_4$, Li_2FeSiO_4). To highlight recent trends in modeling work in this area, we focus on the topical iron phosphate system.

$LiFePO_4$: Defects and Ion Transport

The olivine-structured orthophosphate $LiFePO_4$ has become a highly promising cathode material for use in lithium-ion batteries because of its electrochemical performance (high operating voltage; large theoretical gravimetric capacity), as well as its low cost and safety advantages.[40–48] The $LiFePO_4$ olivine structure (Figure 8) consists of PO_4 tetrahedra with Fe^{2+} ions on corner-sharing octahedral positions and Li^+ ions on edge-sharing octahedral positions, the latter running parallel to the *b*-axis.

After simulating the observed orthorhombic structure, atomistic simulation studies[49] suggest that the most favorable intrinsic defect in $LiFePO_4$ is the anti-site defect, for which a small population (<2%) of Li^+ and Fe^{2+} ions is expected to exchange sites, which we also find for other olivines such as $LiMPO_4$ (M = Mn, Co, Ni);[50] this defect

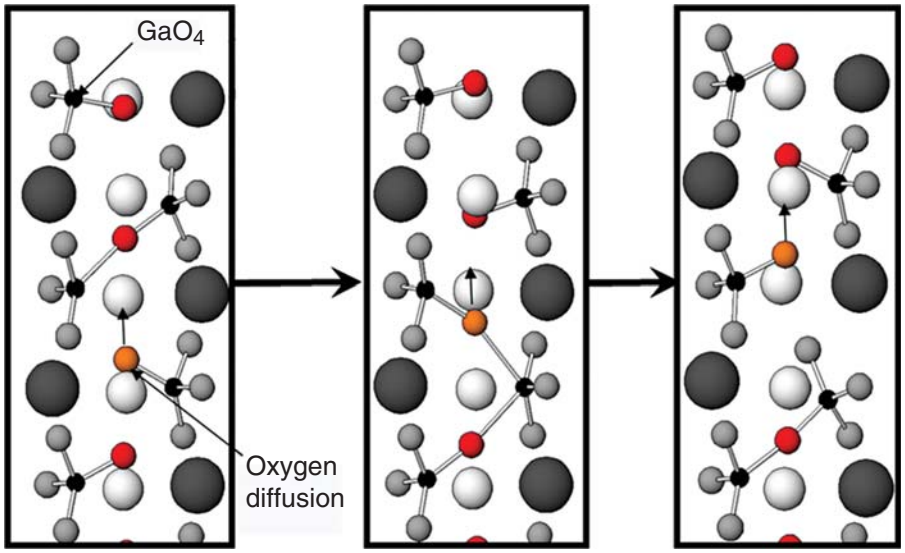

Figure 7. Lowest energy pathway for oxygen vacancy migration in $La_{0.8}Ba_{1.2}GaO_{3.9}$. Snapshots taken from atomistic simulations show that the migration mechanism involves the formation and breaking of Ga_2O_7 units. The migrating oxide ions are highlighted as orange and red spheres, and the stick bonds are drawn to aid the interpretation of the transport mechanism.[39] Key for atom spheres: La (white); Ba (large black); Ga (small black); O (grey).

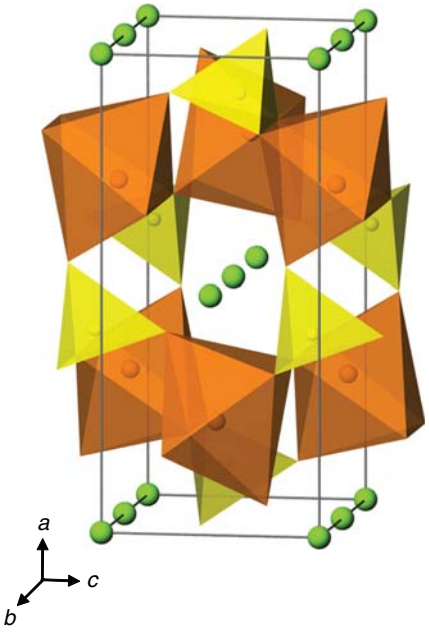

Figure 8. Olivine-type structure of $LiFePO_4$ showing Li ions (green spheres), PO_4 tetrahedra (yellow), and FeO_6 octahedra (orange).

would be temperature dependent and hence sensitive to experimental synthesis conditions. Structural analysis of hydrothermally synthesized $LiFePO_4$ suggests 3 mol% Fe on the lithium sites,[47] while a recently reported scanning transmission electron microscopy (STEM) study[51] has observed anti-site defects in $LiFePO_4$, quoting a concentration of around 1 mol%. In the mineralogy field, this type of anti-site defect or inter-site exchange has been discussed in relation to olivine silicates such as $MgFeSiO_4$ and $MnFeSiO_4$.[52]

Examination of the intrinsic Li ion mobility in $LiFePO_4$ is of vital interest when considering its use as a cathode material in lithium batteries. Modeling studies suggest that lithium-ion diffusion follows a nonlinear, curved trajectory down the [010] channel (Figure 9), with a relatively low migration energy (0.5 eV).[49] High barriers for other pathways indicate that lithium ions cannot readily span the large jump (>4.5 Å) between channels.

This one-dimensional transport mechanism is consistent with the strongly anisotropic nature of the orthorhombic olivine structure and with DFT-type calculations.[53] More recently, neutron diffraction measurements of $LiFePO_4$ (Reference 54) confirm one-dimensional Li^+ diffusion, with a curved migration pathway between adjacent lithium sites, in excellent agreement with earlier predictions.

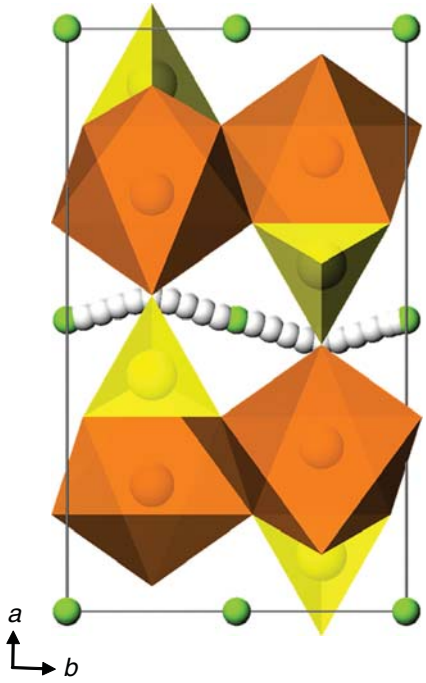

Figure 9. Schematic of the $LiFePO_4$ structure in the *ab* plane showing the calculated curved pathway (white) for Li ion migration in the [010] direction. Li ions (green spheres), PO_4 tetrahedra (yellow), and FeO_6 octahedra (orange).

$LiFePO_4$: Surfaces and Morphology

The formation of $LiFePO_4$ particles of submicron or nanometer size is thought to enhance electrochemical performance by reducing transport path lengths, as well as being important for the electrode/electrolyte interface.[6,7,55] It is also clear that morphological control of nanocrystalline materials is becoming increasingly important.

Given the significance of surface structure and (nano)particle morphology on the properties of $LiFePO_4$, knowledge of these features on the atomic level would provide valuable information for understanding electrochemical mechanisms. The variety of synthesis techniques, however, makes it difficult to extract such fundamental detail or identify distinct surface planes by experiment alone.

As with bulk simulations, advanced atomistic methods can be used to examine surface structures and crystal morphologies. First, relaxed surface structures and energies were calculated for 19 low index planes of $LiFePO_4$.[56] The surface structures exhibit a complex, uneven topology on account of the different sizes of the three constituent moieties, Li^+, Fe^{2+}, and PO_4^{3-}. The majority of the surfaces undergo considerable relaxation, which confirms that the surface chemistry and electrochemical activity cannot be reliably predicted by assuming rigid, unrelaxed terminations of the bulk lattice.

Almost all of the low-energy surfaces are lithium-deficient relative to the bulk lattice, requiring Li vacancies at the surface; this may become increasingly important for Li intercalation with decreasing size of the crystalline particles. The calculated growth morphology (shown in Figure 10) is terminated by {010}, {100}, and {101} faces, which are expected to play a significant role in the electrochemical properties of the material. The crystal shape is anisotropic, with an elongated hexagonal prism-like shape capped by {010} faces; this morphology is consistent with some SEM images of pure $LiFePO_4$,[57] although different synthesis routes have produced a variety of crystallite morphologies,[55,58] such as hexagonal platelets and block-type shapes.

The exposure of the (010) surface is significant since it is normal to the most facile pathway for lithium-ion conduction (along the [010] channel) and hence important for the reversible insertion/de-insertion of lithium ions. The (010) surface may also be important in relation to studies of the $LiFePO_4/FePO_4$ boundary interface. SEM images of plate-like crystallites of uncoated $LiFePO_4$ from hydrothermal synthesis exhibiting large (010) faces[58] have been reproduced by our methods for direct comparison (shown in Figure 11). This reduction in diffusion path length of lithium ions is expected to enhance the electrochemical performance of a cathode prepared from such a material.

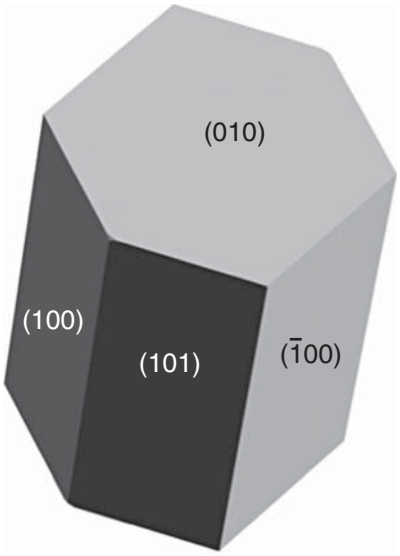

Figure 10. Simulated crystal (growth) morphology of $LiFePO_4$ showing an elongated hexagonal prism shape capped by (010) faces.[56]

Concluding Remarks

This article aimed to demonstrate the valuable role that advanced computational techniques play in contemporary studies of energy-related materials for solid oxide fuel cells (SOFCs) and rechargeable lithium batteries. Such atomic-scale modeling acts as a kind of "virtual microscope" on a complex solid-state world, providing deeper insight based on quantitative results as opposed to qualitative hand-waving arguments. In particular, the simulations have unraveled unique mechanistic detail on ion conduction, defect association, and surface structures with strong links to complementary experimental techniques.

Future studies are likely to encompass (1) new SOFC ion conductors based on oxide structures with flexible tetrahedral units and on multilayered heterostructures with interface effects; (2) next-generation lithium battery electrodes based on nanostructured materials and a better understanding of nanoionics; and

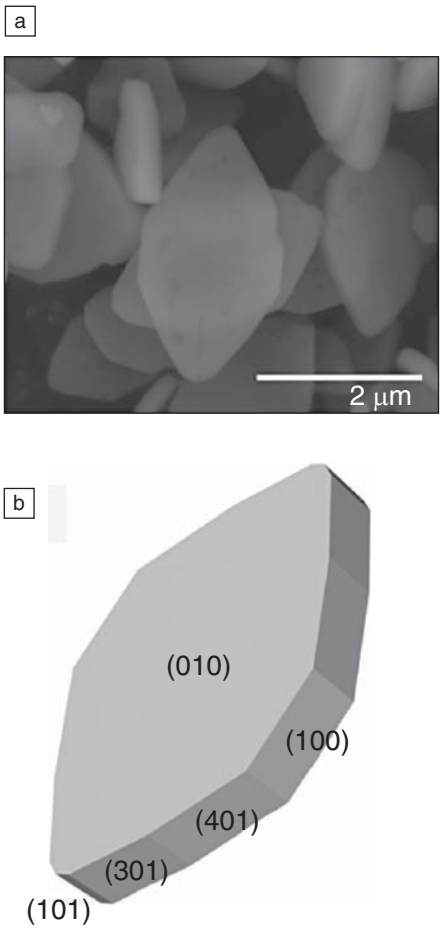

Figure 11. Calculated and experimental plate-like morphologies of $LiFePO_4$;[56] (a) scanning electron microscopy micrograph of noncoated $LiFePO_4$ crystallites from hydrothermal synthesis; (b) simulated morphology.

(3) extension of molecular dynamics and electronic structure techniques to more complex systems (assisted by the continuing growth in supercomputer power). Whatever the future direction, it is clear that major advances in clean energy technologies depends on exploring new materials and concepts and on a greater understanding of the fundamental science of solid-state ionics.

Acknowledgments

The work has been supported by the EPSRC, the SUPERGEN Energy Storage consortium, and the HPCx/HECToR Materials Chemistry Consortium. The authors are grateful for valuable contributions from C.A.J. Fisher, E. Kendrick, J. Kendrick, J. Tolchard, A. Jones, G. Mather, J.D. Gale, and T.J. Richardson.

References

1. M.S. Islam, *J. Mater. Chem*. **17**, 3069 (2007).
2. D.J.L. Brett, A. Atkinson, N.P. Brandon, S.J. Skinner, *Chem. Soc. Rev*. **37**, 1568 (2008).
3. A. Atkinson, S. Barnett, R.J. Gorte, J.T.S. Irvine, A.J. McEvoy, M. Mogensen, S.C. Singhal, J. Vohs., *Nat. Mater*. **3**, 17 (2004).
4. J.M. Tarascon, M. Armand, *Nature* **414**, 359 (2001).
5. M. Armand, J.M. Tarascon, *Nature* **451**, 652 (2008).
6. A.S. Arico, P.G. Bruce, B. Scrosati, J.M. Tarascon, W. Van Schalkwijk, *Nat. Mater*. **4**, 366 (2005).
7. M.S. Whittingham, *Chem. Rev*. **104**, 4271 (2004).
8. C.R.A. Catlow, Ed., *Computer Modelling in Inorganic Crystallography* (Academic Press, San Diego, 1997).
9. W. Koch, M.C. Holthausen, *A Chemist's Guide to Density Functional Theory* (Wiley-VCH, Weinheim, 2001).
10. J.D. Gale, *J. Chem. Soc., Faraday Trans*. **93**, 629 (1997).
11. W. Smith, T.R. Forester, *J. Mol. Graphics* **14**, 136 (1994).
12. G. Kresse, J. Furthmüller, *Phys. Rev. B* **54**, 11169 (1996).
13. M.C. Payne, M.P. Teter, D.C. Allan, T.A. Arias, J.D. Joannopoulos, *Rev. Mod. Phys*. **64**, 1045 (1992).
14. K.D. Kreuer, S.J. Paddison, E. Spohr, M. Schuster, *Chem. Rev*. **104**, 4637 (2004).
15. T. Norby, M. Wideroe, R. Glockner, Y. Larring., *Dalton Trans*. **19**, 3012 (2004).
16. M.S. Islam, R.A. Davies, J.D. Gale, *Chem. Mater*. **13**, 2049 (2001).
17. J.A. Kilner, *Solid State Ionics* **129**, 13 (2000).
18. T. Norby, *J. Mater. Chem*. **11**, 11 (2000).
19. R.J. Phillips, N. Bonanos, F.W. Poulsen, E.O. Ahlgren, *Solid State Ionics*, **125**, 389 (1999).
20. E. Fabbri, S. Licoccia, E. Traversa, E.D. Wachsman, *Fuel Cells*, **9**, 128 (2009).
21. G.C. Mather, F.M. Figueiredo, J.R. de Paz, S. Garcia-Martin, *Inorg. Chem*. **47**, 921 (2008).
22. R. Hempelmann, C. Karmonik, T. Matzke, M. Cappadonia, U. Stimming, T. Springer, M.A. Adams, *Solid State Ionics* **77**, 152 (1995).
23. M.S. Islam, R.A. Davies, *J. Mater. Chem*. **14**, 86 (2004).
24. A. Jones, M.S. Islam, *J. Phys. Chem. C* **112**, 4455 (2008).
25. S. Nakayama, Y. Higuchi, Y. Kondo, M. Sakamoto, *Solid State Ionics* **170**, 219 (2004).
26. J.E.H. Sansom, D. Richings, P.R. Slater, *Solid State Ionics* **139**, 205 (2001).
27. A. Najib, J.E.H. Sansom, J.R. Tolchard, P.R. Slater, M.S. Islam, *Dalton Trans*. 3106 (2004).
28. E. Kendrick, M.S. Islam, P.R. Slater, *J. Mater. Chem*. **17**, 3104 (2007).
29. L. Leon-Reina, J.M. Porras-Vasquez, E.R. Losilla, M.A.G. Aranda, *J. Solid State Chem*. **180**, 1250 (2007).
30. L. León-Reina, E.R. Losilla, M. Martínez-Lara, S. Bruque, M.A.G. Aranda, *J. Mater. Chem*. **14**, 1142 (2004).
31. H. Yoshioka, Y. Nojiri, S. Tanase, *Solid State Ionics* **179**, 2165 (2008).
32. P.J. Panteix, E. Bechade, I. Julien, P. Abelard, D. Bernache-Assollant, *Mater. Res. Bull*. **43**, 1223 (2008).
33. J.R. Tolchard, M.S. Islam, P.R. Slater, *J. Mater. Chem*. **13**, 1956 (2003).
34. J.E.H. Sansom, J.R. Tolchard, D. Apperley, M.S. Islam, P.R. Slater, *J. Mater. Chem*. **16**, 1410 (2006).
35. A. Jones, M.S. Islam, P.R. Slater, *Chem. Mater*. **20**, 5055 (2008).
36. E. Kendrick, M.S. Islam, P.R. Slater, *Chem. Commun*. 715 (2008).
37. R. Haugsrud, T. Norby, *Nat. Mater*. **5**, 193 (2006).
38. F. Schönberger, E. Kendrick, M.S. Islam, P.R. Slater, *Solid State Ionics* **176**, 2951 (2005).
39. E. Kendrick, J. Kendrick, K.S. Knight, M.S. Islam, P.R. Slater, *Nat. Mater*. **6**, 871 (2007).
40. A.K. Padhi, K.S. Nanjundaswamy, J.B. Goodenough, *J. Electrochem. Soc*. **144**, 1188 (1997).
41. N. Ravet, Y. Chouinard, J.F. Magnan, S. Besner, M. Gauthier, M. Armand, *J. Power Sources* **97–98**, 503 (2001).
42. S.Y. Chung, J.T. Bloking, Y.M. Chiang, *Nat. Mater*. **1**, 123 (2002).
43. P. Subramanya Herle, B. Ellis, N. Coombs, L.F. Nazar, *Nat. Mater*. **3**, 147 (2004).
44. C. Delacourt, L. Laffont, R. Bouchet, C. Wurm, J.B. Leriche, M. Morcrette, J.M. Tarason, C. Masquelier, *J. Electrochem. Soc*. **152**, A913 (2005).
45. H. Gabrisch, J.D. Wilcox, M.M. Doeff, *Electrochem. Solid-State Lett*. **9**, A360 (2006).
46. R. Amin, P. Balaya, J. Maier, *Electrochem. Solid-State Lett*. **10**, A13 (2007).
47. J. Chen, M.J. Vacchio, S. Wang, N. Chernova, P.Y. Zavalij, M.S. Whittingham, *Solid State Ionics* **178**, 1676 (2008).
48. T. Muraliganth, A.V. Murugan, A. Manthiram, *J. Mater. Chem*. **18**, 5661 (2008).
49. M.S. Islam, D.J. Driscoll, C.A.J. Fisher, P.R. Slater, *Chem. Mater*. **17**, 5085 (2005).
50. C.A.J. Fisher, V.M. Hart Prieto, M.S. Islam, *Chem. Mater*. **20**, 5907 (2008).
51. S.Y. Chung, S.Y. Choi, T. Yamamoto, Y. Ikuhara, *Phys. Rev. Lett*. **100**, 125502 (2008).
52. C.M.B. Henderson, K.S. Knight, S.A.T. Redfern, B.J. Wood, *Science* **271**, 1713 (1996).
53. D. Morgan, A. Van der Ven, G. Ceder, *Electrochem. Solid-State Lett*. **7**, A30 (2004).
54. S. Nishimura, Y. Kobayashi, K. Ohayama, R. Kanno, M. Yashima, Y. Yamaguchi, A. Yamada, *Nat. Mater*. **7**, 707 (2008).
55. B. Ellis, H.K. Wang, W.R.M. Makahnouk, L.F. Nazar, *J. Mater. Chem*. **17**, 3248 (2007).
56. C.A.J. Fisher, M.S. Islam, *J. Mater. Chem*. **18**, 1209 (2008).
57. S. Franger, F. Le Cras, C. Bourbon, C. Benoit, P. Soudan, J. Santos-Peña, *Recent Res. Devel. Electrochem*. **8**, 225 (2005).
58. G. Chen, X. Song, T.J. Richardson, *Electrochem. Solid-State Lett*. **9**, A295 (2006).
59. G.C. Mather, M.S. Islam, *Chem. Mater*. **17**, 1736 (2005). □